atmosphere

MDPI

Article

Seasonal Differences in the Local and Teleconnected Climate Responses to Vegetation Greening in China and India

Min Xiao [1,2,3,4], Miao Yu [1,2,3,4,*] and Shiyang Zhou [5]

[1] State Key Laboratory of Climate System Prediction and Risk Management, Nanjing University of Information Science and Technology, Nanjing 210044, China; 202312010197@nuist.edu.cn
[2] Key Laboratory of Meteorological Disaster, Ministry of Education, Nanjing University of Information Science and Technology, Nanjing 210044, China
[3] Collaborative Innovation Center on Forecast and Evaluation of Meteorological Disasters, Nanjing University of Information Science and Technology, Nanjing 210044, China
[4] Earth System Modeling Center, Nanjing University of Information Science and Technology, Nanjing 210044, China
[5] Key Laboratory of Polar Atmosphere-Ocean-Ice System for Weather and Climate, Ministry of Education, Department of Atmospheric and Oceanic Sciences & Institute of Atmospheric Sciences, Fudan University, Shanghai 200433, China; shiyangzhou25@m.fudan.edu.cn
* Correspondence: yum@nuist.edu.cn; Tel.: +86-137-76503727

Abstract

Based on leaf area index (LAI) and enhanced vegetation index (EVI) datasets, this study systematically analyzes the spatial distribution and temporal variation characteristics of vegetation index trends at the global scale, clarifying the overall pattern of global greening and the seasonal differences in vegetation greening between eastern China and India. Regions with significant greening in China and India were selected as sensitivity zones, and a coupled land–atmosphere model was used to simulate seasonal differences in the climate response to greening. The findings reveal that: (1) Vegetation greening in eastern China is most pronounced in summer, whereas in India, the greening effect is most prominent in autumn; (2) The synergistic greening of both regions induces a year-round cooling effect in southeastern China, whereas northeastern China experiences summer warming and cooling in the other seasons. Furthermore, spring greening in China and India leads to a pronounced and widespread cooling across the mid-to-high latitudes of Eurasia. (3) In terms of precipitation, southwestern China shows an increasing trend in summer rainfall, while southeastern China shows a decreasing trend. In India, synergistic greening leads to spring and summer warming and autumn and winter cooling, with the cooling and increased precipitation effects being most significant in autumn.

Keywords: vegetation greening; China-India region; biogeophysical effect; surface energy balance

Academic Editor: Ioannis Charalampopoulos

Received: 31 March 2026
Revised: 1 May 2026
Accepted: 8 May 2026
Published: 11 May 2026

1. Introduction

Vegetation serves as an important indicator of global climate change [1]. In global change research, vegetation is an important ecological factor. It is not only affected by climate change [2] but also plays an active feedback role in climate change [3], making the study of vegetation-climate interactions a core component of the IGBP (International Geosphere-Biosphere Programme). Research on the climatic effects of vegetation began in the 1970s and 1980s. Over the past 40 years, studies on Land Use and Land Cover Change (LUCC) have shown that the biogeophysical processes of vegetation cover change

primarily affect the exchange of energy, matter, and momentum between the land and atmosphere through vegetation albedo, Bowen ratio, and roughness effects. Changes in vegetation cover can not only influence local climate but also affect regional and global climate by impacting processes such as atmospheric circulation [4–9]. Vegetation is a crucial component of terrestrial ecosystems and an essential part of the global material and energy cycles [10–13]. A deep understanding of the vegetation-climate system contributes to better research on future climate change, as vegetation feedbacks will have a non-negligible impact on it.

Vegetation restoration exerts a significant influence on climate, with vegetation changes at different latitudes and regions giving rise to distinct climatic effects that exhibit notable seasonality and spatial variability. The climatic effects of vegetation restoration differ clearly by latitude. In low-latitude areas, restoring vegetation generally helps reduce climate change; meanwhile, large-scale planting in temperate and high-latitude regions can worsen warming [14]. This latitudinal pattern is further reflected in circulation adjustments; afforestation in the mid-latitudes of the Northern Hemisphere has been shown to induce hemispheric-scale warming and alter global circulation patterns, with modifications in latent and sensible heat fluxes over water-limited regions shifting the northward extent of the tropical rainfall belt [15]. Ge et al. found that different afforestation schemes will produce different climate effects through satellite observations [16]. Vegetation destruction in low-latitude regions may exert far-reaching influence on high-latitude climates through atmospheric teleconnections [8]. Vegetation cover in tropical regions has a cooling effect on local surface temperatures and exhibits regional and seasonal characteristics [17]. Vegetation changes in mid- and high-latitude regions are mainly controlled by temperature and exhibit strong positive feedback on temperature, whereas vegetation changes in tropical and subtropical regions are mainly driven by precipitation, and vegetation feedback on precipitation is weak [18,19]. Forzieri et al. explored the interaction between local climate and leaf area index, showing that global greening increased surface temperatures by increasing vegetation cover in cold and humid regions, while it reduced surface temperatures through plant evaporative cooling in warm regions [20]. Overall, recent greening has decreased the spatial variability of Earth's surface temperature. Cold ecosystems are more susceptible to climate change, while warm regions are more likely to attain climate mitigation through vegetation.

In recent decades, a pronounced global vegetation greening trend has been observed, particularly in China and India-. According to the latest NASA satellite data, China's substantial contribution to global greening stems largely from a series of initiatives aimed at protecting and expanding forests, which account for 42% of its greening area, while in India, 82% of the newly increased greening area results from intensive cultivation of food crops. Both China and India have achieved remarkable progress in vegetation restoration, with their greening areas increasing significantly, placing them at the forefront globally [21]. Vegetation greening in China is the result of the synergistic effects of human activities and climate change, with human activities playing a dominant role. Climate change and human activities have contributed 40% and 60%, respectively, to the increase in vegetation NDVI in China over the past 34 years [22]. China's greening rate from 2001 to 2023 was three times the global average, primarily driven by afforestation, agricultural intensification, and rising CO_2 concentrations [23]. Regionally, initiatives such as the "Three-North Shelterbelt Program" dominate greening in northern China and coastal areas of southern China, while temperature or precipitation serve as the main drivers in Southwest China and Inner Mongolia [24]. The Tibetan Plateau modulates hydrothermal conditions, altering the sensitivity of vegetation to climate. Long-term vegetation greening is driven by climate warming, whereas interannual variability is related to precipitation [25]. In

India, greening is centered on agricultural intensification, with irrigation-driven dry-season cropping being the primary cause [26]. Greening of the Thar Desert results from the westward shift of summer monsoon rainfall, where soil moisture exerts stronger control over vegetation than precipitation [27]. Increased monsoon rainfall enhances soil moisture, promoting greening in the northwestern subcontinent [28]. Over the past two decades, croplands have contributed 86.5% to India's greening [29], and across different agroclimatic zones, soil moisture and evapotranspiration are the main factors controlling vegetation productivity [30].

Influenced by the monsoon region and its unique geographical characteristics, India is a key region in global climatic processes, whereas China is both a sensitive area and one significantly affected by global climate change [31]. Greening in China and India influences regional and global climate, primarily through changes in land–sea thermal contrasts and impacts on monsoon systems and atmospheric circulation. Li et al. indicate that increases in forest area and leaf area index (LAI) from the world's largest afforestation project will cause a regional temperature dipole, with cooling in northern China and warming in southern China. The local and global surface temperature responses to past vegetation cover expansion in China show seasonal differences, and spring vegetation dynamics in China may influence climate at high northern latitudes [32]. The expansion of agricultural land in India weakens the summer monsoon, thereby reducing precipitation in India by 1.5 mm/day [33]. The response of vegetation to seasonal changes in India exhibits a complex spatial pattern, with greening most pronounced during the monsoon season (July–November) [34], while browning is more pronounced in summer and winter [35]. In China, spring is the season with the most significant increase in the mean Normalized Difference Vegetation Index (NDVI) [36]. Southern China maintains high greenness year-round with little seasonal variation. In contrast, northern China shows the strongest summer greening trend.

Numerical simulation provides an important means of quantifying the climatic effects of vegetation change, and the Community Earth System Model (CESM) has become an ideal tool for studying vegetation–climate interactions due to its comprehensive land–atmosphere coupling [37]. Although previous studies have separately examined the climatic effects of vegetation greening in China and India, most have focused on annual mean responses or growing-season analyses, and few have systematically compared the seasonal differences in biophysical climate effects between these two mid-latitude greening hotspots. Given the exceptionally high computational demands of the dynamic vegetation module in Earth system models, most land–atmosphere coupling studies tend to neglect the perturbing effects of temporal vegetation variations on climate [38,39]. However, this study incorporates dynamically varying, satellite-derived leaf area index (LAI) data into a fully coupled land–atmosphere model (CESM), allowing us to explicitly represent the seasonal cycle of vegetation greening and isolate its biophysical effects on surface temperature and precipitation.

Building on the novel contributions described above, the specific objectives of this study are as follows: (1) to characterize the seasonal differences in vegetation greening between China and India; (2) to investigate the seasonal impacts of vegetation greening in China and India on local and remote 2-m temperature and precipitation; (3) to reveal the seasonal differences in the mechanisms underlying the climate responses to vegetation greening in China and India.

2. Materials and Methods

The coupled land-atmosphere model (CESM2.1.3), Community Atmosphere Model version 6.0 (CAM6.0) coupled with Community Land Model version 5.0 (CLM5.0), devel-

oped by the National Center for Atmospheric Research (NCAR), is utilized in this study. The atmospheric module, CAM6 [37], effectively simulates large-scale circulation, climatic variability, and energy balance. The land surface module, CLM5.0, replaces the original River Transport Model (RTM) with the river-routing model of the Model for Scale-Adaptive River Transport (MOSART), providing significant improvements in key dynamic processes, including soil and vegetation hydrology. In this work, the satellite phenology mode, which depicts vegetation coverage using satellite parameters, is used.

The Global Inventory Modeling and Mapping Studies LAI product (GIMMS LAI4g), the Global Land Surface Satellite (GLASS) LAI, and the Long-term Global Mapping (GLOBMAP) version 3 are three satellite datasets of LAI. The MOD13C2 and MYD13C2 Enhanced Vegetation Index (EVI) datasets, derived from the MODIS sensors aboard NASA's Terra (morning overpass) and Aqua (afternoon overpass) satellites, are used to complement the LAI datasets, providing a consistent measure of vegetation greenness that enables cross-validation and enhances the robustness of vegetation trend analyses.

Based on the analysis of vegetation greening distribution in China and India in the second part of the results, the regions marked with red hatching in Figure 1, representing areas with notable greening over the last four decades, were chosen as sensitivity zones for the vegetation greening simulation. The greening zone in China is approximately 2.16 times larger than in India. When comparing the periods 1982–1991 and 2007–2016, the average LAI increase was 0.148 m^2 m^{-2} in China and 0.082 m^2 m^{-2} in India.

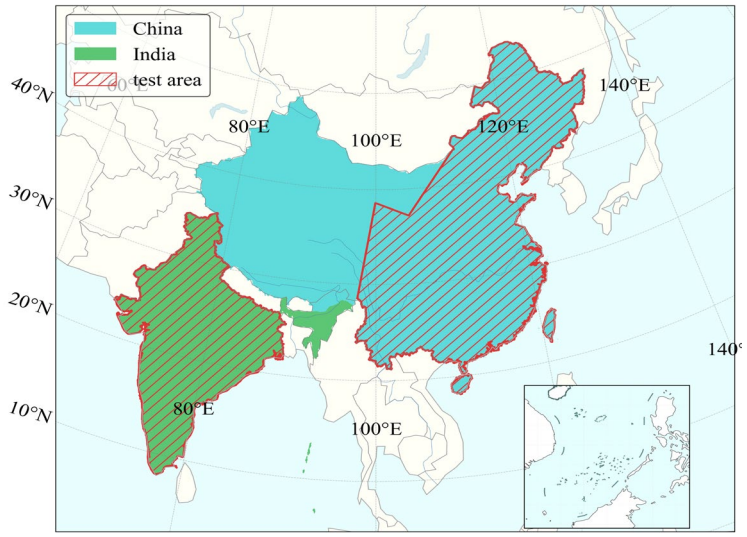

Figure 1. Numerical simulation sensitivity test area.

The numerical simulation approach adopted in this study involves replacing the model's default LAI values with GIMMS LAI4g data, thereby incorporating dynamic LAI values with monthly and interannual variations to represent greening effects. Specifically, the interannual LAI from 1982 to 2020 was applied in the vegetation greening regions of China and India, while LAI values in other regions were maintained at the 1982 level. The simulations were conducted at the global scale with a spatial resolution of 1.9° × 2.5°. Historical sea surface temperature (SST), CO_2 concentration, and other forcing variables were prescribed using climatological mean values to isolate the impact of LAI on climate. Each experiment was run for the period 1980–2020, with the first two years treated as model spin-up, and the results from 1982 to 2020 were used for analysis. The effects of greening were obtained by subtracting the average of the first decade from that of the last decade of the simulation period.

To assess atmospheric heating, this study uses the inversion method from Yanai et al. (1973) to compute the apparent heat source (Q_1) and apparent moisture sink (Q_2) [40], which are then used to determine the total atmospheric heating rate and the latent heating from moisture condensation. The calculation approach is detailed as follows:

$$Q_1 = C_P\left(\frac{p}{p_0}\right)^k\left(\frac{\partial\theta}{\partial t}\right) + v\cdot\nabla\theta + \omega\frac{\partial\theta}{\partial p} \quad (1)$$

$$Q_2 = -L\left(\frac{\partial q}{\partial t}\right) + v\cdot\nabla q + \omega\frac{\partial q}{\partial p} \quad (2)$$

Here, C_p represents the specific heat at constant pressure, and L is the latent heat of condensation; the Poisson constant is denoted by k; and (P_0) = 1000 hPa. The variables P, ν, ω, θ, and q stand for pressure, velocity vector, vertical velocity in p-coordinates, potential temperature, and specific humidity, respectively, while g is the gravitational acceleration. By vertically integrating Q_1 and Q_2 from the surface to the top of the atmosphere, we obtain the total atmospheric apparent heat source $<Q_1>$ and apparent moisture sink $<Q_2>$. A positive $<Q_1>$ indicates net atmospheric heating, whereas a negative value implies net atmospheric cooling. Similarly, a positive $<Q_2>$ denotes a net moisture sink accompanied by the release of latent heat from condensation, while a negative value indicates an increase in moisture content along with evaporative cooling.

In this study, seasons are defined according to standard meteorological conventions: spring (March–May, MAM), summer (June–August, JJA), autumn (September–November, SON), and winter (December–February, DJF). This seasonal division is consistently applied to all datasets and analyses, including the calculation of seasonal vegetation trends, the identification of greening sensitivity zones, and the assessment of seasonal climate responses to vegetation greening. The use of a unified seasonal framework ensures comparability across different observational datasets and model experiments.

3. Results

3.1. Global Temporal and Spatial Changes of Vegetation

Based on three LAI and two EVI observation datasets, this study uses the Mann-Kendall test method to analyze the spatial trends in global vegetation cover from 1987 to 2016. The results indicate that LAI exhibits an increasing trend across most regions of the globe (Figure 2a–c). Combined with the right-skewed probability density distribution (Figure 2f), this further confirms a significant global greening trend. Specifically, the GIMMS LAI dataset shows that areas with a highly significant increasing trend ($p < 0.01$) account for 19.69% of the total land surface, primarily distributed in central North America, western Eurasia, India, and eastern China. In the GLASS LAI dataset, areas with a highly significant increasing trend account for 20.05% and are mainly distributed in northern South America, central Africa, India, and eastern China. In the GLOBMAP LAI dataset, areas with a highly significant increasing trend ($p < 0.01$) account for 41.20%, mainly distributed in northern North America, northern South America, central Africa, northern Eurasia, India, and eastern China. The two EVI datasets (MYD13C2 and MOD13C2) similarly reflect a global vegetation greening trend, with particularly pronounced greening in China and India (Figure 2d,e). Synthesizing results from multiple observational datasets, it is evident that all datasets indicate significant greening in China and India.

The spatially averaged LAI and EVI values in China both exhibit increasing trends. The regression results from the five datasets are statistically significant, with p-values well below 0.05 (Figure 3a). Although the specific magnitudes of increase vary across datasets and the goodness of fit differs, the overall trend is clear: vegetation cover in China improved during this period (Figure 3a). The spatially averaged LAI in India also shows an

increasing trend. Among the three LAI datasets, GLASS exhibits the highest rate of increase and the strongest goodness-of-fit (Figure 3b). Figure 3c presents the regression analysis results for global vegetation cover trends. The GIMMS dataset performs best in revealing the trend in globally spatially averaged LAI from 1980 to 2020, with a strong model fit (R = 0.88) and a statistically significant trend (*p*-value approaching zero). The GLOBMAP dataset also shows a linear relationship, although its goodness-of-fit is relatively low. The regression results for the GLASS dataset also indicate a significant trend. Both LAI and EVI demonstrate a significant greening trend in China and India during the period 1980–2020.

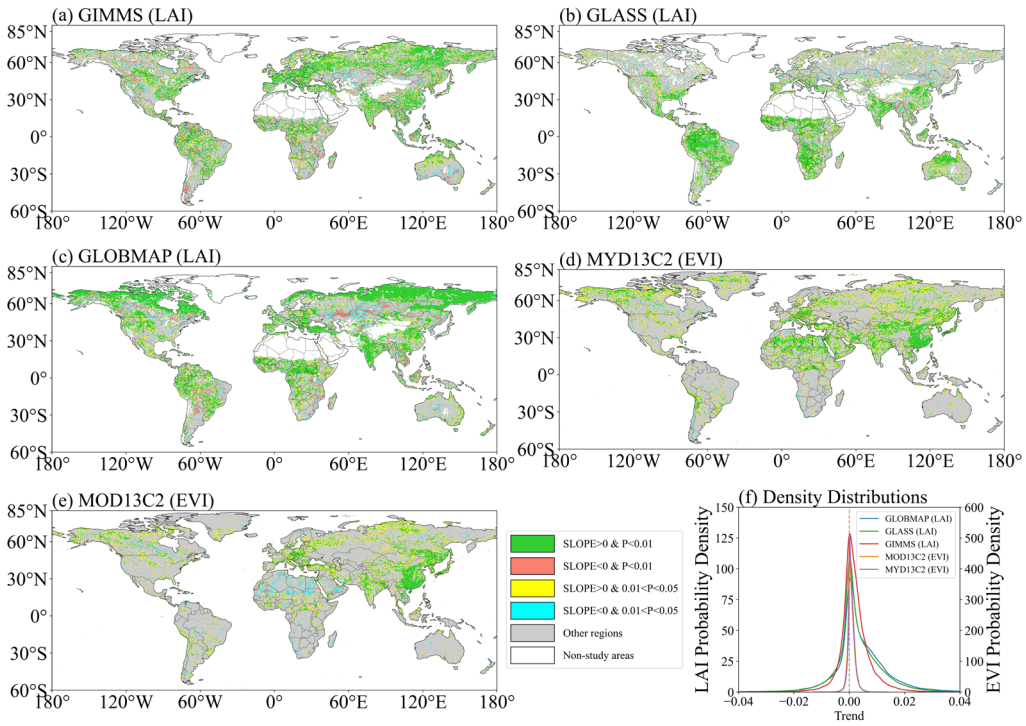

Figure 2. Spatial distribution of global LAI trends from the GIMMS, GLASS, and GLOBMAP datasets (**a**–**c**), spatial distribution of EVI trends from the MYD13C2 and MOD13C2 datasets (**d**,**e**), and probability density distribution (**f**).

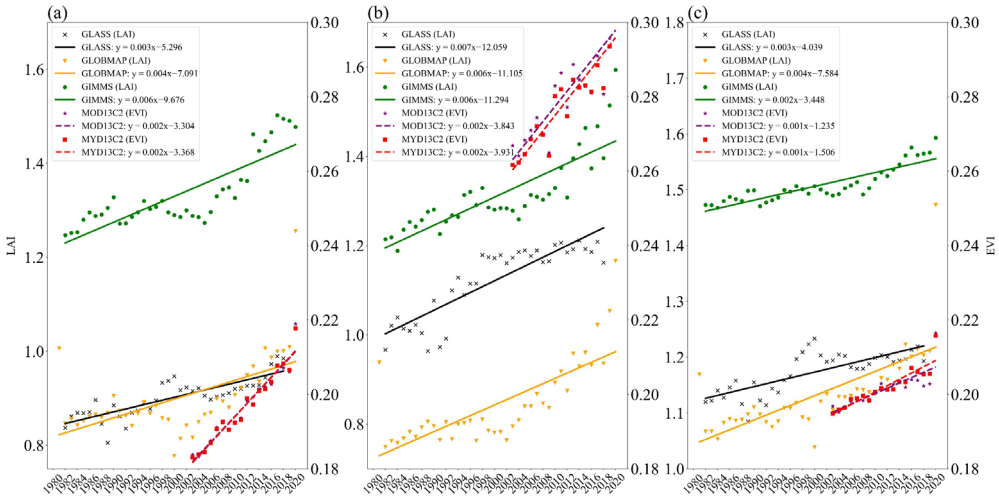

Figure 3. Trends in LAI and EVI in China (**a**), India (**b**), and globally (**c**) during 1980–2020.

3.2. Seasonal Differences in Vegetation Greening Between China and India

As shown in Figure 4, this study analyzes the spatial distribution of seasonal vegetation trends in China and India using three LAI datasets—GIMMS, GLASS, and GLOBMAP.

All three datasets show notable seasonal differences, with summer (JJA) displaying the strongest LAI trends across China and India combined. The spatially averaged increasing trends for the GIMMS, GLASS, and GLOBMAP datasets are 0.0042 m^2 m^{-2} yr^{-1}, 0.007 m^2 m^{-2} yr^{-1}, and 0.018 m^2 m^{-2} yr^{-1}, respectively, with GLOBMAP showing the strongest greening trend, significantly higher than those of the other two datasets. Winter (DJF) shows the weakest LAI trends across the three datasets, with spatially averaged trends of 0.0023 m^2 m^{-2} yr^{-1}, 0.0016 m^2 m^{-2} yr^{-1}, and −0.0036 m^2 m^{-2} yr^{-1} for GIMMS, GLASS, and GLOBMAP, respectively, with GLOBMAP exhibiting a negative trend. In terms of the proportion of areas with significant trends, the GIMMS dataset shows the highest proportion of significant positive trends in spring (42.1%), the GLOBMAP dataset shows the highest proportion in summer (79.2%), and the GIMMS dataset again shows the highest proportions in autumn and winter (36.0% and 36.8%, respectively). Spatially, the strongest annual mean LAI trend in the GIMMS dataset is located in South China (Figure 4a–d), with a trend value of 0.011 m^2 m^{-2} yr^{-1}, while the region with the greatest seasonal variation is Central China (standard deviation of 0.0035), indicating that seasonal changes most strongly influence vegetation growth in this region. The spatial distribution of seasonal trends in the GLOBMAP dataset differs considerably from those in the GIMMS and GLASS datasets, particularly in South China during winter and in India during spring (Figure 4i,l). These discrepancies may arise from differences in sensor sensitivity to vegetation signals, variations in cloud cover and atmospheric correction algorithms, and differences in the calculation methods of vegetation indices across datasets. All three datasets consistently indicate that summer is the most significant season for vegetation greening in China and India, reflecting the dominant role of hydrothermal conditions in vegetation growth. However, notable differences exist among datasets in terms of trend magnitude and spatial distribution, highlighting the value of multi-dataset comparative analysis for a more comprehensive understanding of vegetation change characteristics. Based on the spatial distribution of LAI trends across the three datasets, the areas delineated by the red lines in Figure 4 were selected as the greening sensitivity experiment zones for the numerical simulation.

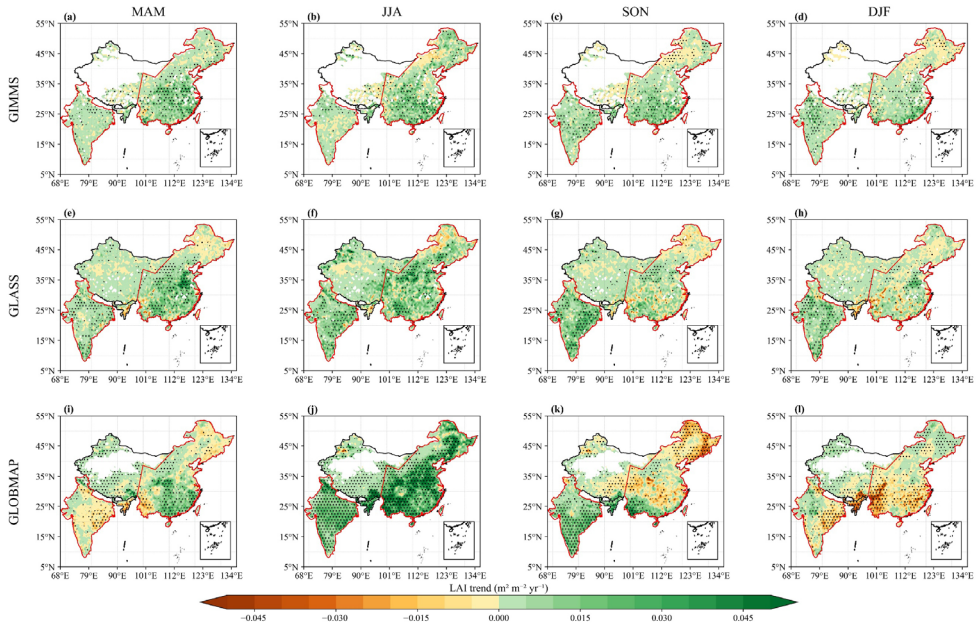

Figure 4. Spatial distribution of seasonal LAI trends in China and India based on the GIMMS (**a**–**d**), GLASS (**e**–**h**), and GLOBMAP (**i**–**l**) datasets (MAM: spring; JJA: summer; SON: autumn; DJF: winter). Stippled areas indicate statistically significant trends at the 95% confidence level based on the MK test.

Based on three LAI datasets, this study performs a seasonal-scale analysis of spatially averaged vegetation trends for China and India as a whole, and for each region individually. For China and India combined, summer exhibits the most pronounced vegetation greening (Figure 5b), with all three datasets showing significant increasing trends ($p < 0.001$). The GLOBMAP dataset shows the strongest increasing trend (0.0155 LAI/yr), significantly higher than GLASS (0.0074 LAI/yr) and GIMMS (0.0048 LAI/yr). In winter, the trends differ across the three datasets: GLOBMAP shows a significant decrease (−0.0035 LAI/yr, $p < 0.001$), whereas GLASS and GIMMS show weak increases (Figure 5d). In spring (MAM) and autumn (SON), the three datasets also exhibit divergent trends: GIMMS shows stable and significant increases in both seasons, while GLOBMAP shows almost no change in autumn (Figure 5a,c). For China alone, summer remains the season with the most significant vegetation growth, with GLOBMAP again showing the highest rate of increase (0.0145 LAI/yr), compared with 0.0071 LAI/yr for GLASS and 0.0058 LAI/yr for GIMMS (Figure 5f). In autumn, neither GLASS (0.0012 LAI/yr, $p = 0.158$) nor GLOBMAP (−0.0030 LAI/yr, $p = 0.053$) shows a significant trend in China, whereas GIMMS maintains a significant increasing trend (0.0045 LAI/yr, $p < 0.001$) (Figure 5g). In winter, GLOBMAP shows a significant decrease in China, GIMMS shows a significant increase, while GLASS shows almost no change (Figure 5h). For India alone, autumn stands out as the season with the most pronounced vegetation greening, with GLASS (0.0109 LAI/yr), GLOBMAP (0.0116 LAI/yr), and GIMMS (0.0055 LAI/yr) all showing highly significant trends ($p < 0.001$) (Figure 5k). Summer also exhibits significant increasing trends, with GLOBMAP showing a particularly high rate of 0.0184 LAI/yr and GLASS reaching 0.0086 LAI/yr, while GIMMS is relatively lower (0.0034 LAI/yr) (Figure 5j). In spring and winter, the three datasets show considerable divergence in vegetation greening trends in India (Figure 5i,l).

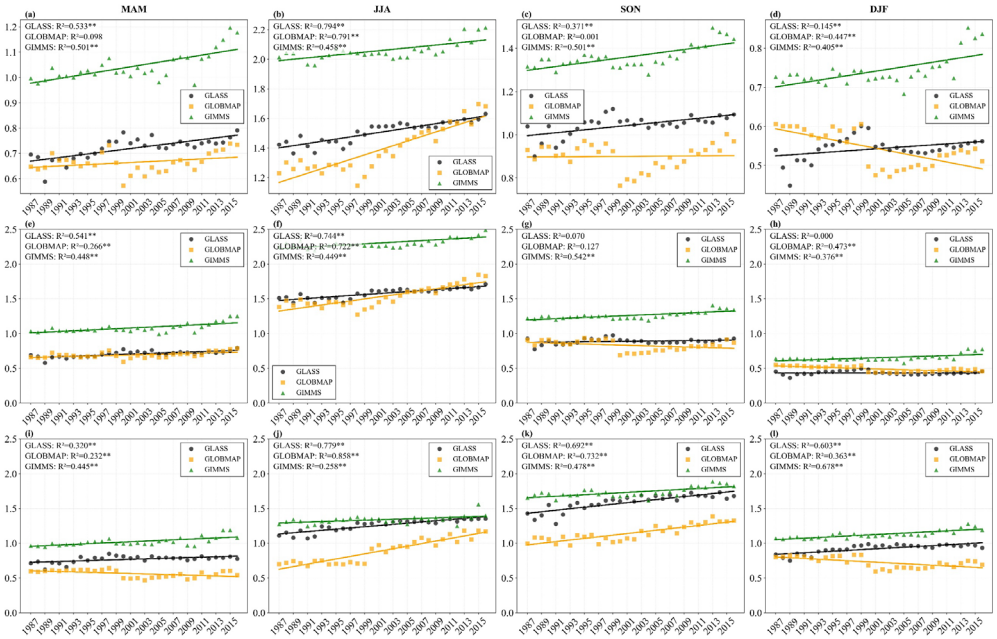

Figure 5. Seasonal LAI variations in China and India combined (**a**–**d**), China alone (**e**–**h**), and India alone (**i**–**l**) with the dashed lines showing their linear trends and double asterisks (**) denoting a statistically significant trend at the 95% confidence level based on the two-tailed *t*-test.

Comprehensive analysis of multi-source data indicates that vegetation changes in China and India exhibit pronounced regional and seasonal differences. The seasonal characteristics of vegetation greening in China and India are reflected in the fact that vegetation growth in China is most pronounced in summer, whereas in India it is most

pronounced in autumn. On average, the greening of China and India as a whole is most pronounced in summer. In terms of spatial distribution, southeastern China shows a stable greening trend, while central China exhibits greater seasonal variability in vegetation. Comparison among datasets reveals that GLOBMAP captures the strongest greening signal in summer across China and India, but shows negative trends in winter and autumn, whereas GIMMS demonstrates relatively stable positive trends across all four seasons, with GLASS falling between the two. GIMMS LAI4g spans the period from 1982 to 2020, offering the longest temporal coverage. In climate model simulations, the use of forcing data with long time series enhances the model's ability to simulate vegetation–climate interactions, offering distinct advantages, particularly for the study of long-term vegetation responses to climate change. Owing to its seasonal stability across all four seasons, long temporal coverage, and statistical significance, the GIMMS LAI4g dataset emerges as the optimal choice for replacing the default LAI values in the CESM model. Using the GIMMS LAI4g dataset in CESM, with LAI values that include both monthly and interannual variability in a coupled land–atmosphere model, can effectively reduce input data uncertainty and enhance the ability of numerical simulations to capture vegetation characteristics dynamics.

3.3. Seasonal Response of 2-m Temperature and Precipitation

The effects of vegetation greening in China and India on 2-m temperature show clear seasonal differences. Globally, among grid cells showing a cooling response, spring and winter account for the highest proportions, both around 65%. Within the greening sensitivity experiment zones, southeastern China consistently experiences cooling across all four seasons (Figure 6). Northeastern China cools every season except summer, when it warms. In India, warming occurs in spring and summer (Figure 6a,c), while cooling happens in autumn and winter (Figure 6b,d). During spring, widespread significant cooling is visible across the mid-to-high latitudes of Eurasia (Figure 6a), making it the main cooling region for that season and one of the strongest cooling centers of the year. The east-central United States shows significant warming, whereas western Europe and central South America exhibit weak cooling (Figure 6a). In summer, cooling persists over parts of Eurasia's mid-to-high latitudes but with less intensity than in spring (Figure 6b). Central South America and southern Africa show localized weak cooling. A small area of significant cooling appears in southwestern China, while a large region of significant warming forms in the Caspian Sea, contrasting with spring's cooling in that region (Figure 6b). In autumn, significant cooling occurs in eastern Eurasia, northern South America, and the Middle East, while extensive warming is seen across North America, western Eurasia, and northeastern Asia (Figure 6c). In winter, Eurasia's mid-to-high latitudes again show the most extensive and intense cooling, similar to spring but not passing the confidence level test. Southern North America experiences significant cooling, while northern Africa and western North America show significant warming effects (Figure 6d).

The global precipitation response to vegetation greening in China and India exhibits pronounced seasonal differences, with the spatial distribution of precipitation responses showing stronger localization than that of temperature effects (Figure 7). In terms of precipitation responses outside greening regions, spring shows significant precipitation decreases over Greenland, while widespread increases occur across Europe and northern South America (Figure 7a). In summer, precipitation decreases significantly across central and western Eurasia, whereas significant increases appear over southern Africa (Figure 7b). In autumn, precipitation increases further over southern Africa, while it decreases significantly over central Africa (Figure 7c). In winter, significant precipitation increases occur over southern North America and Australia. Although certain signals

are present in some remote regions, the model's overall remote precipitation response exhibits considerable uncertainty, with signal stability substantially lower than that for temperature (Figure 7d). Within the greening sensitivity experiment zones, precipitation responses in summer and autumn are particularly pronounced in China and India (Figure 7b,c). In India, local precipitation decreases in spring and winter, with the decrease intensifying in northern India during summer while southern India shifts to increased precipitation; in autumn, widespread significant increases occur across India (Figure 7c). In the Chinese greening experiment zone, precipitation responses are relatively dispersed, with southeastern China showing precipitation increases in all seasons except summer (Figure 7b).

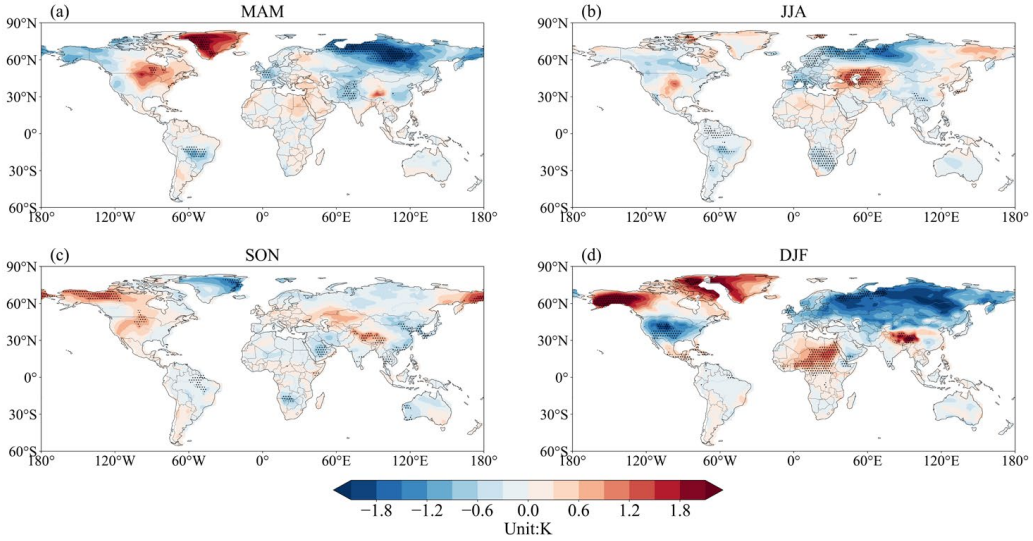

Figure 6. Seasonal differences in the global 2-m temperature response to vegetation greening in China and India ((**a**): spring, (**b**): summer, (**c**): autumn, (**d**): winter). The response values are calculated as the difference between the 2011–2020 average and the 1982–1991 average. Stippled areas indicate statistical significance at the 95% confidence level based on the *t*-test.

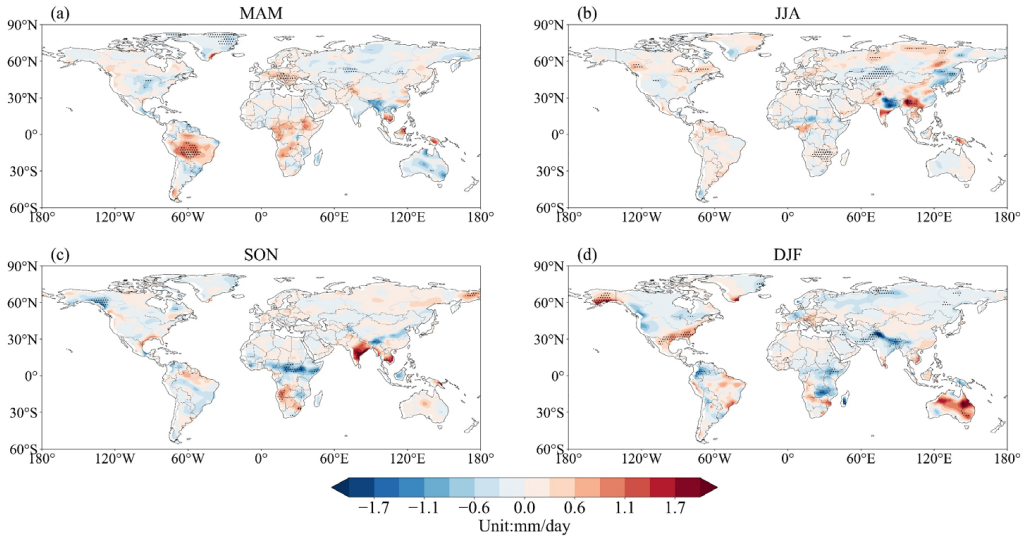

Figure 7. Seasonal differences in the global precipitation response to vegetation greening in China and India ((**a**): spring, (**b**): summer, (**c**): autumn, (**d**): winter). The response values are calculated as the difference between the 2011–2020 average and the 1982–1991 average. Stippled areas indicate statistical significance at the 95% confidence level based on the *t*-test.

3.4. Seasonal Response of Surface Energy Fluxes

Changes in vegetation cover significantly influence radiation transfer and surface energy balance by modulating underlying surface properties such as albedo, roughness, and soil moisture, thereby altering local temperature and precipitation distributions. Surface net radiation (R_n) is partitioned among sensible heat (SH), latent heat (LH), and ground heat flux (G), following the relationship $R_n = SH + LH + G$. A portion of the net radiation energy is exchanged with the atmosphere in the form of sensible and latent heat, while the remainder is transferred to the soil layer through soil heat conduction.

As shown in Figure 8, we present the spatial distribution of local responses in surface net radiation (Rn), sensible heat flux (SH), latent heat flux (LH), and vertically integrated total cloud cover (CLDTOT) induced by vegetation greening in China and India. Due to seasonal differences in vegetation greening, the surface energy balance also exhibits pronounced seasonal variations. In southern China, greening leads to increased albedo and cloud cover across all seasons (Figure 8m–t), which together result in a significant reduction in surface net radiation (Figure 8a–d), thereby driving local cooling. Concurrently, soil moisture in this region shows an increasing trend throughout the year (Figure 8u–x), further enhancing evaporative cooling. Notably, a net radiation increase occurs in parts of southeastern China during summer (Figure 8b); this anomaly arises from a decrease in total cloud cover (CLDTOT) (Figure 8n), although the increased radiative energy is released more as latent heat (Figure 8j). In summary, the net radiation reduction caused by increased albedo and cloud cover, combined with evaporative cooling from elevated soil moisture and enhanced latent heat release, constitutes the core physical process underlying the stable cooling response in southern China across all seasons, clearly explaining the seasonal consistency of the cooling effect in this region. As discussed previously, the GIMMS LAI4g dataset shows that northeastern China experiences the most significant summer greening (Figure 4b). This region exhibits a warming effect in summer (in stark contrast to the cooling effect in other seasons). The key mechanism is that summer in northeastern China features significantly reduced soil moisture (Figure 8v), limiting evaporative cooling; concurrently, cloud cover decreases markedly (Figure 8n) with no significant change in albedo (Figure 8r). Together, these factors lead to an increase in surface net radiation (Figure 8b), ultimately producing a distinct summer warming pattern that differs from other seasons.

India, significantly increased autumn soil moisture (Figure 8w), combined with reduced surface net radiation (Figure 8c) caused by increased cloud cover (Figure 8o), results in overall autumn cooling. In winter, Indian soil moisture remains relatively high (Figure 8w); under the joint regulation of albedo (Figure 8t) and cloud cover (Figure 8p), net radiation increases across most of the region (Figure 8d). However, the surplus surface energy is released more as latent heat flux (Figure 8l), and evaporative cooling offsets radiative warming, so a cooling response still dominates winter in India. In spring and summer, clear regional differentiation appears in near-surface air temperature over India. In spring, southern India is dominated by reduced albedo (Figure 8q), leading to increased surface net radiation (Figure 8a) and significantly rising local temperatures. In contrast, northern India is controlled by increased albedo (Figure 8q), resulting in reduced net radiation (Figure 8a) and ultimately a cooling signature. In summer, although albedo increases markedly across north-central India (Figure 8r), the regulation effect of decreased cloud cover is stronger (Figure 8n), dominating the increase in surface net radiation (Figure 8b), which in turn causes significant summer warming across north-central India.

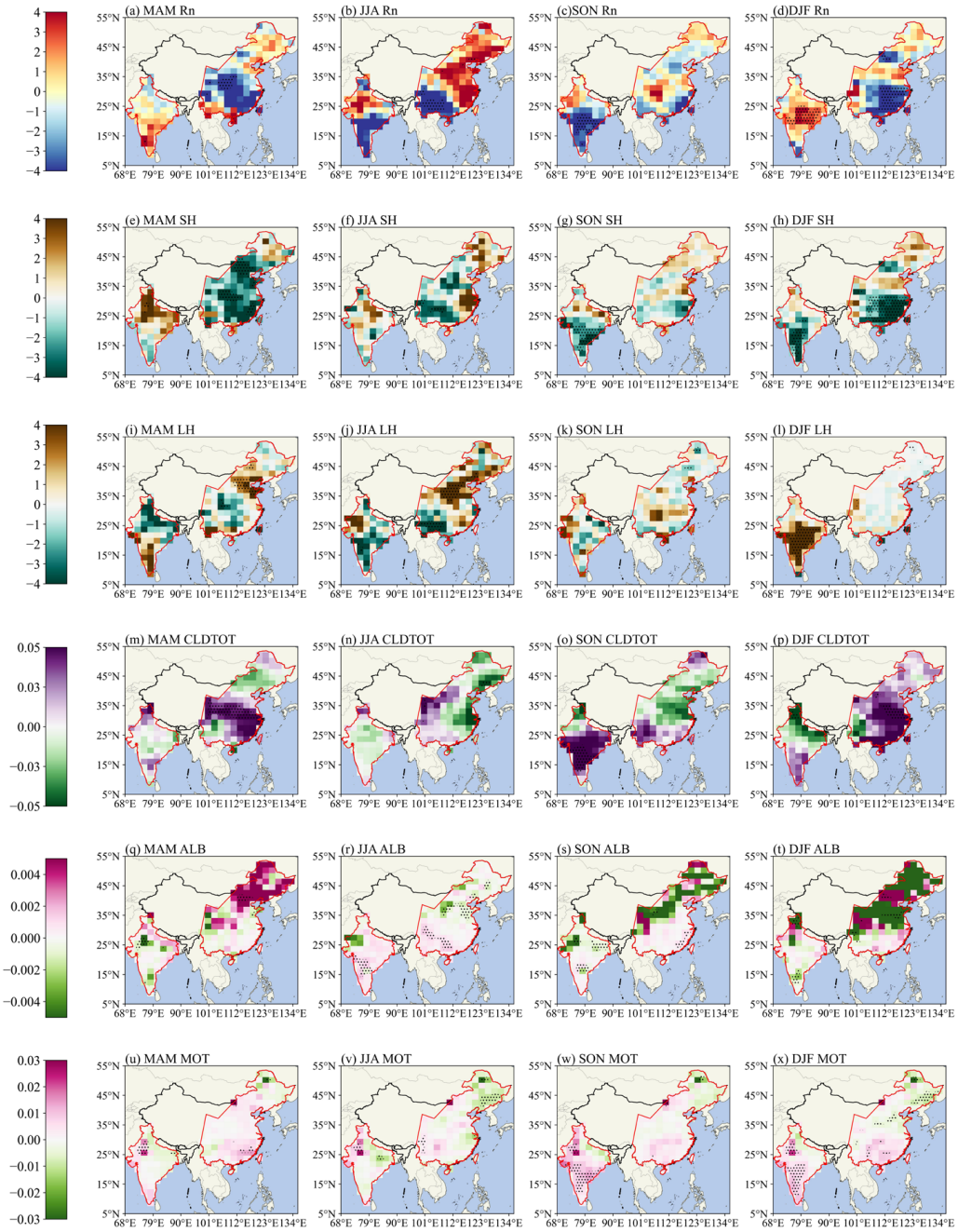

Figure 8. Seasonal responses of (**a**–**d**) net radiation (R_n), (**e**–**h**) sensible heat flux (SH), (**i**–**l**) latent heat flux (LH), (**m**–**p**) total cloud cover (CLDTOT), (**q**–**t**) albedo and (**u**–**x**) soil moisture due to greening in China and India—columns from left to right: spring, summer, autumn, and winter, respectively. Response values are calculated as the difference between the 2011–2020 average and the 1982–1991 average. Stippled areas indicate statistical significance at the 90% confidence level based on the *t*-test.

3.5. Seasonal Response of Apparent Heat Source and Apparent Moisture Sink

Based on the surface energy budget characteristics described above, we further analyze the impacts of greening in China and India on the local column-integrated apparent heat source (<Q_1>) and apparent moisture sink (<Q_2>) (Figure 9). As core parameters characterizing atmospheric diabatic heating and moisture budgets, the responses of these two variables are directly associated with the energy and moisture processes induced by vegetation greening, exhibiting pronounced regional and seasonal differences.

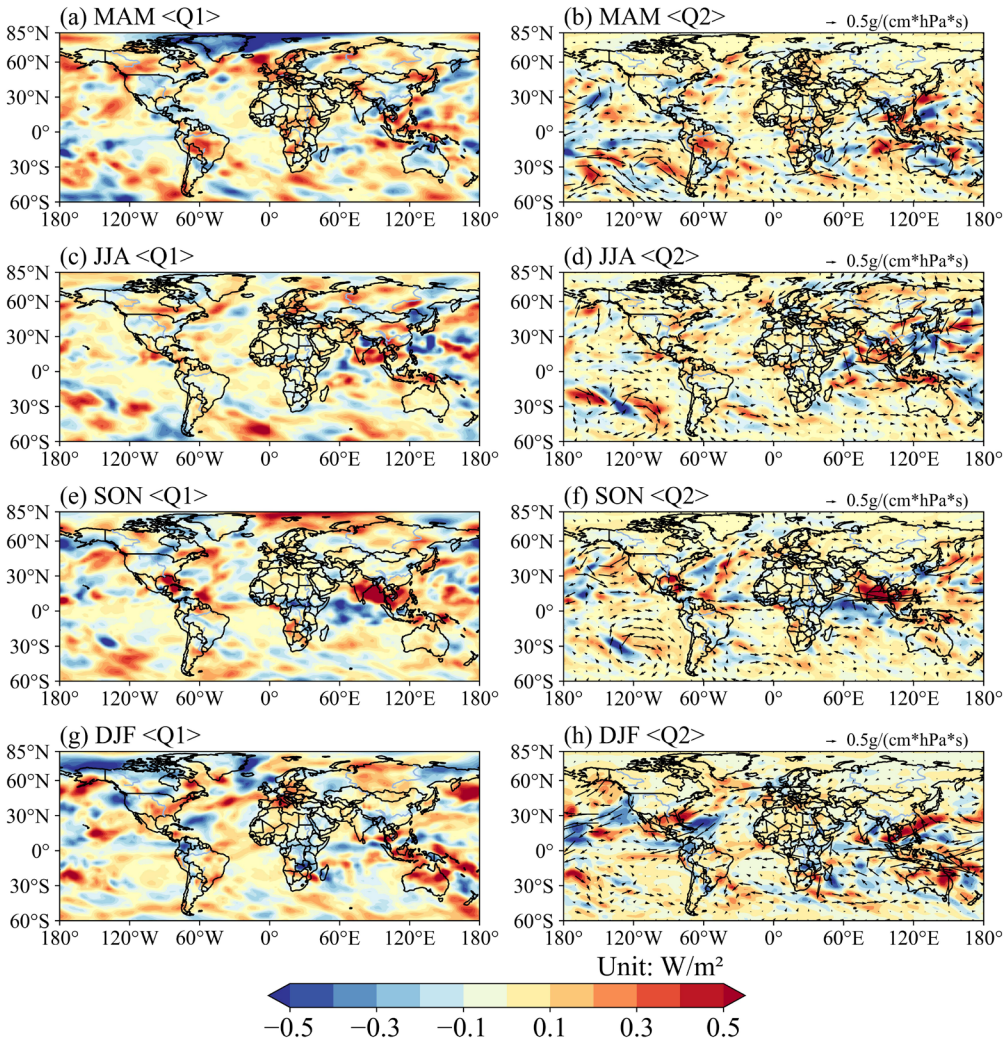

Figure 9. Seasonal responses of (**left column**) the vertically integrated apparent heat source, <Q_1>, and (**right column**) apparent moisture sink, <Q_2>, due to the greening in China and India. Rows from top to bottom represent spring, summer, autumn, and winter, respectively. Arrows denote water vapor flux. Response values are calculated as the difference between the 2011–2020 average and the 1982–1991 average.

Autumn is the most pronounced season for vegetation greening in India (Figure 4c), during which intense vegetation transpiration transports substantial water vapor into the atmosphere. However, increased local evapotranspiration does not necessarily lead to increased local precipitation—the key factor is whether the water vapor can effectively condense and form precipitation. In autumn, the vertically integrated apparent water vapor sink (<Q_2>) and apparent heat source (<Q_1>) over India are significantly enhanced (Figure 9e,f), indicating substantial local water vapor condensation. This phenomenon arises from the synergistic effects of two factors. First, significantly increased autumn soil moisture over India (Figure 8w), combined with reduced surface net radiation caused by increased cloud cover (Figure 8o,c), favors the maintenance of a high-humidity near-surface environment and promotes convective development. Second, concurrent vegetation greening in China, which is also in a significant period, contributes to cross-regional moisture transport; although some water vapor is still transported downstream from India in autumn, local condensation processes become dominant. The spatial distribution of the vertically integrated apparent water vapor sink (<Q_2>) over India closely matches the spatial pattern of regional precipitation, further confirming the indicative value of <Q_2> as a core parameter of the atmospheric moisture budget. Strong vegetation transpiration supplies a

moisture source, which, combined with favorable thermal and dynamic conditions, enables substantial local condensation and precipitation formation over India during autumn.

Compared with the Indian region, the response characteristics of$<Q_1>$ and $<Q_2>$ over China exhibit different seasonal and spatial patterns. In summer, $<Q_2>$ over southeastern China shows a decreasing trend, indicating weakened water vapor condensation (Figure 9d). In contrast, during all seasons except summer, the vertically integrated apparent water vapor sink increases across southeastern China, with substantial water vapor condensation and cloud droplet formation occurring. In spring, autumn, and winter, surface net radiation over southeastern China decreases due to increased albedo and cloud cover (Figure 8a,c,d), resulting in stable cooling; meanwhile, soil moisture shows an increasing trend (Figure 8u,w,x), and $<Q_2>$ is significantly enhanced (Figure 9b,f,h). Together, these three factors create an environment favorable for precipitation. In summer, however, total cloud cover over this region does not increase but rather decreases (Figure 8n), leading to an increase in surface net radiation (Figure 8b) and a decreasing trend in $<Q_2>$ (Figure 9d), thereby suppressing water vapor condensation. Although vegetation transpiration can still supply moisture, it cannot easily be converted into precipitation. In spring and winter, the magnitude of moisture budget changes over China is relatively small, and the responses of $<Q_1>$ and $<Q_2>$ are comparatively moderate. In summer and autumn, by contrast, the moisture response over China is stronger, with more pronounced changes in $<Q_1>$ and $<Q_2>$. This characteristic is highly correlated with the seasonal pattern of vegetation greening in China. Vegetation greening in China is most significant in summer and autumn, during which vegetation transpiration exerts a notable regulatory effect on local water vapor, thereby directly influencing the diabatic heating process of $<Q_1>$ and the moisture budget balance of $<Q_2>$.

3.6. Adjustment of the Atmospheric Circulation

The core mechanism by which vegetation greening in China and India influences climate in the mid-to-high latitudes of the Northern Hemisphere and remote regions lies in the alteration of local surface energy budgets and evapotranspiration, triggering significant geopotential height anomalies and circulation adjustments across different tropospheric levels, with the intensity and propagation path of this signal exhibiting a pronounced seasonal dependence. In spring and winter, the 2-m temperature and circulation responses in the teleconnected regions are significantly stronger than those in summer and autumn (Figure 10). Taking spring as an example, greening in China and India enhances evapotranspiration, inducing local surface cooling and generating negative geopotential height anomalies over East Asia at the lower troposphere (850 hPa) (Figure 10a). Acting as a Rossby wave source, this anomalous perturbation propagates westward upstream and into high latitudes along the westerly jet stream, forming a quasi-stationary Rossby wave train spanning the Northern Hemisphere. This wave train is significantly intensified at the upper troposphere (200 hPa), manifesting as negative geopotential height anomalies over the mid-to-high latitudes of Eurasia and positive anomalies over Greenland and North America (Figure 10c). Under this circulation configuration, the mid-to-high latitudes of Eurasia, dominated by low-pressure anomalies and cold advection, experience widespread 2-m temperature decreases; in contrast, Greenland and eastern North America, controlled by high-pressure anomalies, exhibit significant local warming due to the combined effects of subsidence-induced warming and warm advection (Figure 6a). The circulation pattern in winter is highly similar to that in spring—a strong positive geopotential height anomaly dominates the Arctic region, while negative anomalies prevail over Eurasia and North America, resulting in a consistent "cool Eurasia, warm North America" pattern in the 2-m temperature response (Figure 10j–l). In contrast, the intensity of circulation teleconnection

signals is substantially weaker in summer and autumn. In summer, owing to a marked increase in net surface radiation, the greening regions in China and India exhibit positive geopotential height anomalies at the lower troposphere (850 hPa) (Figure 10d). After ascending to the upper troposphere (200 hPa), these positive anomalies shift their center northward and excite an alternating positive–negative wave train downstream along the westerlies, notably with regions near the Caspian Sea controlled by positive geopotential height anomalies (Figure 10f) and showing significantly elevated 2-m temperatures (Figure 6b), representing a specific pathway through which summer greening influences mid-latitude climate.

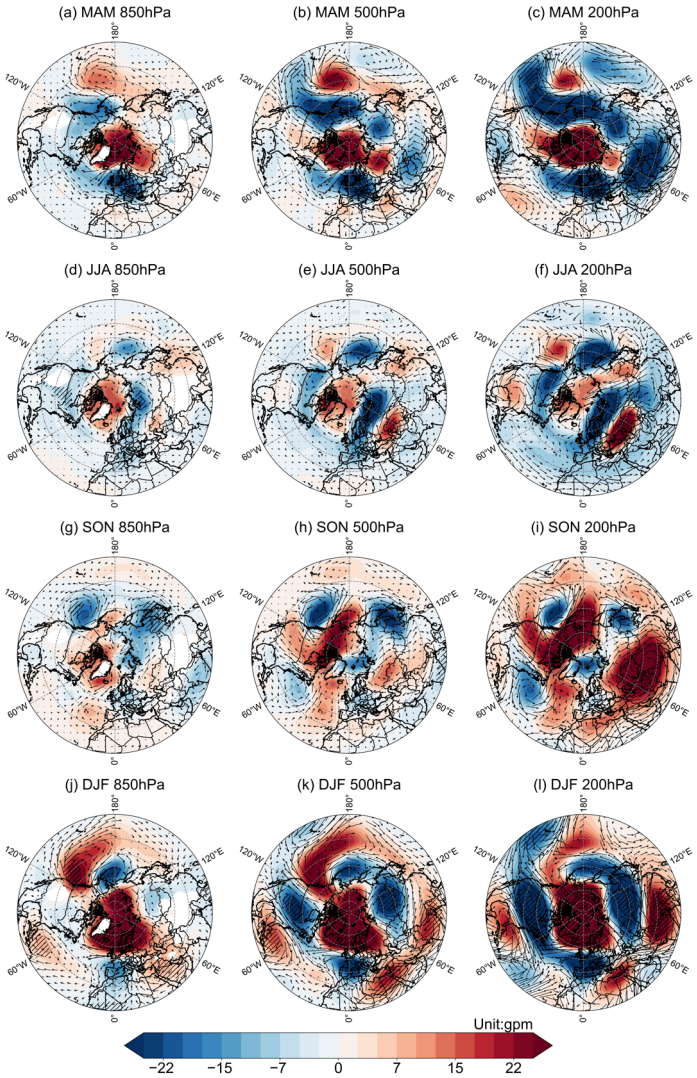

Figure 10. Seasonal responses of geopotential height at (**left column**) 850 hPa, (**middle column**) 500 hPa, and (**right column**) 200 hPa due to greening in China and India. Rows from top to bottom represent spring, summer, autumn, and winter, respectively. Arrows denote UV wind fields. Response values are calculated as the difference between the 2011–2020 average and the 1982–1991 average.

4. Discussion and Conclusions

Based on LAI and EVI datasets, this study systematically analyzes the spatial distribution and temporal variation characteristics of vegetation index trends from a global perspective, clarifying the overall pattern of global greening and the seasonal differences in greening between China and India. Although there are minor discrepancies in the magnitude of vegetation index increases across different datasets, the overall spatial pattern of greening is highly consistent. From a spatial distribution perspective, the regions with

significant global greening are mainly concentrated in central North America, western Eurasia, eastern China, and India (Figure 2), which is highly consistent with the findings of Chen et al. From a temporal perspective, vegetation growth in China is most significant in summer (Figure 5f). In contrast, in India, the greening effect is most pronounced in autumn (Figure 5k), consistent with previous studies that found it concentrated during the monsoon season [34]. Regarding spatial heterogeneity, distinct differences exist in LAI growth characteristics across eastern China: southeastern China exhibits a stable LAI increasing trend, while central China shows greater seasonal variability in vegetation (Figure 4).

The greening processes in China and India exert significant regulatory effects on regional temperature, with pronounced regional and seasonal differences. In Southeast China, vegetation greening induces stable cooling across all four seasons; in Northeast China, cooling occurs in all seasons except summer, which shows warming; while in India, the pattern features a north–south dipole in spring (cooling in the north and warming in the south), mid–northern warming in summer, and overall cooling in autumn and winter (Figure 6). In remote regions, large-scale cooling appears over the mid- and high-latitude Eurasia in spring, warming over western Asia in summer, cooling over eastern Eurasia in autumn, and again strong cooling over the mid- and high-latitude Eurasia in winter (Figure 6). For precipitation, the local responses are more concentrated: in India, spring and winter precipitation decreases, summer precipitation decreases in the north, but increases in the south, and autumn precipitation increases markedly; in Southeast China, precipitation increases in all seasons except summer (Figure 7). Compared with the 2-m temperature response, the impact of greening on precipitation in China and India is more complex, and the spatial distribution of the precipitation response is more scattered. This is consistent with the findings of Yu et al., who noted that vegetation greening in China is most prominent in the eastern region, and that the regulation of precipitation by vegetation is influenced by multiple factors such as moisture transport and topographic conditions, resulting in a clear spatial differentiation of the precipitation response [41].

In southern China, increases in albedo and cloud cover reduce net radiation in all seasons (Figure 8m–t), while rising soil moisture enhances evaporative cooling (Figure 8u–x), leading to stable cooling (Figure 6). In Northeast China, summer soil moisture and cloud cover decrease significantly (Figure 8n,v), and net radiation increases (Figure 8b), causing summer warming that contrasts with cooling in the other seasons. In India, autumn cooling is driven by increased soil moisture and cloud cover (Figure 8w,o); winter net radiation increases, but the energy is released as latent heat, still resulting in cooling. In spring, cooling in northern India is caused by increased albedo (Figure 8q), while the opposite occurs in southern India; in summer, reduced cloud cover over mid-northern India dominates the increase in net radiation (Figure 8r), producing warming (Figure 8). In summary, the net local temperature effect of greening is determined by the relative strength of radiative and non-radiative processes and their seasonal variations.

Autumn is the most pronounced season for Indian greening (Figure 4c). Vegetation transpiration delivers large amounts of water vapor, and both $<Q_1>$ and $<Q_2>$ are significantly enhanced (Figure 9e,f), indicating active local water vapor condensation. This benefits from the increase in local soil moisture (Figure 8w), the increase in cloud cover (Figure 8o) that reduces net radiation (Figure 8c), and the cross-regional moisture transport induced by concurrent greening in China. Together, these factors make local water vapor condensation dominant. In China, during summer, $<Q_2>$ decreases in the southeastern region, suppressing water vapor condensation (Figure 9d). In spring, autumn, and winter, increased albedo and cloud cover in the southeast reduce net radiation (Figure 8a,c,d), while soil moisture remains high (Figure 8u,w,x), and $<Q_2>$ is enhanced (Figure 9b,f,h), favoring precipitation formation.

The teleconnection responses in spring and winter are significantly stronger than those in summer and autumn (Figure 10). In spring, local cooling induced by greening excites negative geopotential height anomalies in the lower troposphere over East Asia. These perturbations propagate along the westerly jet stream, forming a Rossby wave train across the Northern Hemisphere, resulting in cooling over mid- and high-latitude Eurasia and warming over Greenland and eastern North America (Figures 6a and 10a,c). The winter circulation pattern resembles that of spring, exhibiting a "cold Eurasia—warm North America" configuration (Figure 10j–l). In summer, increased surface net radiation shifts the lower troposphere to positive geopotential height anomalies, which propagate upward and excite a downstream wave train, causing warming in regions such as the Caspian Sea (Figures 6b and 10d,f). In summary, greening in China and India can exert significant remote modulation on mid- and high-latitude climates by exciting season-dependent Rossby wave trains.

This study is subject to several limitations. Simulations rely on a single land–atmosphere model, and uncertainties in cloud schemes, land surface processes and sea surface temperatures may distort the magnitude and spatial pattern of climate responses, especially in remote regions. In addition, our greening experiments only address bio-physical impacts and neglect carbon-related biogeochemical feedbacks. Furthermore, this study focuses specifically on the one-way impact of vegetation greening on climate and does not investigate the reverse pathway. Further studies using multi-model ensembles, higher resolution and improved vegetation dynamics will help reduce uncertainties and strengthen the credibility of vegetation–climate simulations. Future research should also aim to explore the bidirectional interactions between vegetation and climate over China and India to better understand the coupled vegetation–climate system. The findings of this study provide important insights into the mechanisms of regional vegetation–climate interactions and offer a scientific basis for ecological environmental construction and climate adaptation management in China and India.

Author Contributions: Conceptualization, M.X. and M.Y.; methodology, M.X., M.Y. and S.Z.; software, M.X.; validation, M.X.; investigation, M.X. and M.Y.; data curation, M.X.; writing—original draft preparation, M.X.; writing—review and editing, M.X. and M.Y.; visualization, M.X.; supervision, M.Y. All authors have read and agreed to the published version of the manuscript.

Funding: Funding support for this study was provided by the National Key R&D Program of China, Project No. 2025YFF0812000 and 2025YFF0812003, and the National Natural Science Foundation of China (U2442207).

Data Availability Statement: The GLOBMAP LAI (Version 3) data are openly available in Zenodo at https://zenodo.org/records/4700264 (accessed on 10 June 2024). The GIMMS LAI4g data is openly available at https://doi.org/10.5281/zenodo.7649107 (accessed on 19 October 2024). The GLASS LAI data are available at http://www.glass.umd.edu/ (accessed on 10 June 2024). MODIS EVI data (MOD13C2 and MYD13C2) are available from the NASA MODIS Land Products at https://modis.gsfc.nasa.gov/data/dataprod/mod13.php (accessed on 19 June 2024).

Acknowledgments: We acknowledge the High Performance Computing Platform of Nanjing University of Information Science & Technology for supporting this work.

Conflicts of Interest: The authors declare no conflicts of interest.

Abbreviations

The following abbreviations are used in this manuscript:

LAI	Leaf Area Index
EVI	Enhanced Vegetation Index
CESM	The Community Earth System Model

GIMMS	The Global Inventory Modeling and Mapping Studies
GLASS	The Global Land Surface Satellite
GLOBMAP	The Long-term Global Mapping
Q_1	The apparent heat source
Q_2	The apparent moisture sink

References

1. Wang, Q.; Zhang, Q.-P.; Zhou, W. Grassland Coverage Changes and Analysis of the Driving Forces in Maqu County. *Phys. Procedia* **2012**, *33*, 1292–1297. [CrossRef]
2. Ali, M. Effects of Climate Change on Vegetation. In *Climate Change Impacts on Plant Biomass Growth*; Springer: Dordrecht, The Netherlands, 2013; pp. 29–49.
3. Zeng, Z.; Piao, S.; Li, L.Z.X.; Zhou, L.; Ciais, P.; Wang, T.; Li, Y.; Lian, X.; Wood, E.F.; Friedlingstein, P.; et al. Climate mitigation from vegetation biophysical feedbacks during the past three decades. *Nat. Clim. Change* **2017**, *7*, 432–436. [CrossRef]
4. Alkama, R.; Cescatti, A. Biophysical climate impacts of recent changes in global forest cover. *Science* **2016**, *351*, 600–604. [CrossRef] [PubMed]
5. Bonan, G.B. Forests and Climate Change: Forcings, Feedbacks, and the Climate Benefits of Forests. *Science* **2008**, *320*, 1444–1449. [CrossRef]
6. Neelin, J.D.; Su, H. Moist Teleconnection Mechanisms for the Tropical South American and Atlantic Sector. *J. Clim.* **2005**, *18*, 3928–3950. [CrossRef]
7. Snyder, P.; Delire, C. A Systematic Analysis of the Influence of Vegetation on Local and Global Climate Using a Coupled Atmosphere-Biosphere Model, CCM3-IBIS. In *AGU Fall Meeting Abstracts*; American Geophysical Union: Washington, DC, USA, 2001; Volume 0125.
8. Voldoire, A.; Royer, J.F. Tropical deforestation and climate variability. *Clim. Dyn.* **2004**, *22*, 857–874. [CrossRef]
9. Voldoire, A.; Royer, J.F. Climate sensitivity to tropical land surface changes with coupled versus prescribed SSTs. *Clim. Dyn.* **2005**, *24*, 843–862. [CrossRef]
10. Fan, X.; Ma, Z.; Yang, Q.; Han, Y.; Mahmood, R.; Zheng, Z. Land use/land cover changes and regional climate over the Loess Plateau during 2001–2009. Part II: Interrelationship from observations. *Clim. Change* **2015**, *129*, 441–455. [CrossRef]
11. Pielke, R.A.; Pitman, A.; Niyogi, D.; Mahmood, R.; McAlpine, C.; Hossain, F.; Goldewijk, K.K.; Nair, U.; Betts, R.; Fall, S.; et al. Land use/land cover changes and climate: Modeling analysis and observational evidence. *WIREs Clim. Change* **2011**, *2*, 828–850. [CrossRef]
12. Seneviratne, S.I.; Corti, T.; Davin, E.L.; Hirschi, M.; Jaeger, E.B.; Lehner, I.; Orlowsky, B.; Teuling, A.J. Investigating soil moisture–climate interactions in a changing climate: A review. *Earth-Sci. Rev.* **2010**, *99*, 125–161. [CrossRef]
13. Zheng, Y.; Kumar, A.; Niyogi, D. Impacts of land–atmosphere coupling on regional rainfall and convection. *Clim. Dyn.* **2015**, *44*, 2383–2409. [CrossRef]
14. Betts, R.A.; Falloon, P.D.; Goldewijk, K.K.; Ramankutty, N. Biogeophysical effects of land use on climate: Model simulations of radiative forcing and large-scale temperature change. *Agric. For. Meteorol.* **2007**, *142*, 216–233. [CrossRef]
15. Swann, A.L.S.; Fung, I.Y.; Chiang, J.C.H. Mid-latitude afforestation shifts general circulation and tropical precipitation. *Proc. Natl. Acad. Sci. USA* **2012**, *109*, 712–716. [CrossRef]
16. Ge, J.; Guo, W.; Pitman, A.J.; De Kauwe, M.G.; Chen, X.; Fu, C. The Nonradiative Effect Dominates Local Surface Temperature Change Caused by Afforestation in China. *J. Clim.* **2019**, *32*, 4445–4471. [CrossRef]
17. Osborne, T.M.; Lawrence, D.M.; Slingo, J.M.; Challinor, A.J.; Wheeler, T.R. Influence of vegetation on the local climate and hydrology in the tropics: Sensitivity to soil parameters. *Clim. Dyn.* **2004**, *23*, 45–61. [CrossRef]
18. Liu, Z.; Notaro, M.; Kutzbach, J.; Liu, N. Assessing global vegetation-climate feedbacks from observations. *J. Clim.* **2006**, *19*, 787–814. [CrossRef]
19. Notaro, M.; Liu, Z.; Williams, J.W. Observed vegetation-climate feedbacks in the United States. *J. Clim.* **2006**, *19*, 763–786. [CrossRef]
20. Forzieri, G.; Alkama, R.; Miralles, D.G.; Cescatti, A. Satellites reveal contrasting responses of regional climate to the widespread greening of Earth. *Science* **2017**, *356*, 1180–1184. [CrossRef]
21. Zhu, Z.; Piao, S.; Myneni, R.B.; Huang, M.; Zeng, Z.; Canadell, J.G.; Ciais, P.; Sitch, S.; Friedlingstein, P.; Arneth, A.; et al. Greening of the Earth and its drivers. *Nat. Clim. Change* **2016**, *6*, 791–795. [CrossRef]
22. Jin, K.; Wang, F.; Han, J.Q.; Shi, S.; Ding, W. Contribution of climatic change and human activities to vegetation NDVI change over China during 1982–2015. *Acta Geogr. Sin.* **2020**, *75*, 961–974. [CrossRef]
23. Wei, S.; Li, X.; Wang, K.; Wang, T.; Piao, S. Two decades of persistent greening in China despite 2023 climate extremes. *Sci. China Earth Sci.* **2025**, *68*, 1064–1073. [CrossRef]

24. Song, W.; Feng, Y.; Wang, Z. Ecological restoration programs dominate vegetation greening in China. *Sci. Total Environ.* **2022**, *848*, 157729. [CrossRef]
25. Li, Z.Y.; Yang, Q.; Ma, Z.G.; Chen, L.; Zhang, L. Responses of vegetation to climate change and human activities in the arid and semiarid regions of northern China. *Chin. J. Atmos. Sci.* **2024**, *48*, 859–874. [CrossRef]
26. Park, T.; Gumma, M.K.; Wang, W.; Panjala, P.; Dubey, S.K.; Nemani, R.R. Greening of human-dominated ecosystems in India. *Commun. Earth Environ.* **2023**, *4*, 419. [CrossRef]
27. Kashyap, R.; Kuttippurath, J.; Patel, V.K. Agriculture intensification and moisture-induced Thar desert greening: Implications for energy balance, socio-economy, and biodiversity. *GISci. Remote Sens.* **2025**, *62*, 2483458. [CrossRef]
28. Jin, Q.; Wang, C. The greening of Northwest Indian subcontinent and reduction of dust abundance resulting from Indian summer monsoon revival. *Sci. Rep.* **2018**, *8*, 4573. [CrossRef] [PubMed]
29. Kuttippurath, J.; Kashyap, R. Greening of India: Forests or Croplands? *Appl. Geogr.* **2023**, *161*, 103115. [CrossRef]
30. Samykannu, V.; Goroshi, S.; Palanisamy, R.; Pai, D.; Mohapatra, M. Seasonal NDVI shifts: Assessing vegetation responses to hydro-climatic changes across diverse agro-climatic zones of India. *Remote Sens. Appl. Soc. Environ.* **2026**, *41*, 101882. [CrossRef]
31. Zhang, W.; Zhou, T. Increasing impacts from extreme precipitation on population over China with global warming. *Sci. Bull.* **2020**, *65*, 243–252. [CrossRef] [PubMed]
32. Li, Y.; Piao, S.; Chen, A.; Ciais, P.; Li, L.Z.X. Local and teleconnected temperature effects of afforestation and vegetation greening in China. *Natl. Sci. Rev.* **2020**, *7*, 897–912. [CrossRef]
33. Chou, C.; Ryu, D.; Lo, M.-H.; Wey, H.-W.; Malano, H.M. Irrigation-induced land–atmosphere feedbacks and their impacts on Indian summer monsoon. *J. Clim.* **2018**, *31*, 8785–8801. [CrossRef]
34. Sur, K.; Verma, V.K.; Panwar, P.; Shukla, G.; Chakravarty, S.; Nath, A.J. Monitoring vegetation degradation using remote sensing and machine learning over India–a multi-sensor, multi-temporal and multi-scale approach. *Front. For. Glob. Change* **2024**, *7*, 1382557. [CrossRef]
35. Tiwari, R.; Gupta, D.K.; Chauhan, P.K.; Prajapati, S.; Singh, A.K. Spatio-Temporal Variability of NDVI Over Indian Continents. In Proceedings of the 2024 URSI Regional Conference on Radio Science (URSI-RCRS), Bhimtal, India, 22–25 October 2024; pp. 1–4. [CrossRef]
36. Piao, S.; Fang, J. Seasonal Changes in Vegetation Activity in Response to Climate Changes in China between 1982 and 1999. *Acta Geogr. Sin.* **2003**, *58*, 119–125. [CrossRef]
37. Danabasoglu, G.; Lamarque, J.; Bacmeister, J.; Bailey, D.A.; DuVivier, A.K.; Edwards, J.; Emmons, L.K.; Fasullo, J.; Garcia, R.; Gettelman, A.; et al. The Community Earth System Model Version 2 (CESM2). *J. Adv. Model. Earth Syst.* **2020**, *12*, E2019MS001916. [CrossRef]
38. Peng, C. From static biogeographical model to dynamic global vegetation model: A global perspective on modelling vegetation dynamics. *Ecol. Model.* **2000**, *135*, 33–54. [CrossRef]
39. Peng, S.-S.; Piao, S.; Zeng, Z.; Ciais, P.; Zhou, L.; Li, L.Z.X.; Myneni, R.B.; Yin, Y.; Zeng, H. Afforestation in China cools local land surface temperature. *Proc. Natl. Acad. Sci. USA* **2014**, *111*, 2915–2919. [CrossRef]
40. Yanai, M.; Esbensen, S.; Chu, J.-H. Determination of bulk properties of tropical cloud clusters from large-scale heat and moisture budgets. *J. Atmos. Sci.* **1973**, *30*, 611–627. [CrossRef]
41. Yu, L.; Liu, Y.; Liu, T.; Yan, F. Impact of recent vegetation greening on temperature and precipitation over China. *Agric. For. Meteorol.* **2020**, *295*, 108197. [CrossRef]